

# Collective Oxygen Transport in Tetragonal Ta<sub>2</sub>O<sub>5</sub>

Sung-Hoon Lee<sup>1,\*</sup> and Ki-Ha Hong<sup>2,†</sup>

<sup>1</sup>*Department of Applied Physics, Kyung Hee University, Yongin, Korea*

<sup>2</sup>*Department of Materials Science and Engineering,  
Hanbat National University, Daejeon, Korea*

## Abstract

In crystalline materials, atomic motion is generally confined to vibrations within a fixed lattice, with significant movement beyond vibrations usually associated with defect migration. Here, we present the discovery of collective ionic transport within the tetragonal phase of tantalum pentoxide (Ta<sub>2</sub>O<sub>5</sub>), a material whose atomic structure has long been a mystery. Through density functional theory calculations, we have definitively determined its atomic structure to be a four-fold screw-symmetric configuration derived from the orthorhombic phase of Ta<sub>2</sub>O<sub>5</sub>. Remarkably, ab-initio molecular dynamics simulations of this structure reveal that specific oxygen atoms undergo collective, floating movements at temperatures as low as a few hundred degrees Celsius, even in the absence of defects. The calculated energy barrier for this motion is exceptionally low (0.2 eV), attributed to extensive structural relaxation around the oxygen transport pathways and the resulting dynamic charge rebalancing. These findings elucidate the previously unexplained high oxygen conductivity in tetragonal Ta<sub>2</sub>O<sub>5</sub> and provide new insights for designing materials with enhanced atomic mobility.

---

\* [lsh@khu.ac.kr](mailto:lsh@khu.ac.kr)

† [kiha.hong@hanbat.ac.kr](mailto:kiha.hong@hanbat.ac.kr)

## INTRODUCTION

Crystalline solids are typically characterized by their highly ordered and static atomic arrangement within a repeating unit cell, forming a crystal lattice. Generally, it has been assumed that below their melting or sublimation points, the positions of these atoms remain fixed, experiencing only vibrations around their equilibrium positions. This conventional understanding suggests that ionic conduction in crystalline materials can occur only through defects, such as vacancies or interstitial sites.<sup>1-3</sup> This concept underpins solid-state materials science, particularly solid-state ionics, which depends on ionic conduction within crystalline materials. However, the present study finds that this basic assumption does not hold for the tetragonal phase of Ta<sub>2</sub>O<sub>5</sub>.

Ta<sub>2</sub>O<sub>5</sub> is a technologically important material due to its high dielectric constant and wide bandgap, making it suitable for applications such as high-k dielectrics,<sup>4-6</sup> resistive random access memory,<sup>7-9</sup> photo- and electrocatalysis,<sup>10,11</sup> and antireflection coatings.<sup>12</sup> It exists in two primary crystalline phases: the orthorhombic L-Ta<sub>2</sub>O<sub>5</sub> at lower temperatures and the tetragonal H-Ta<sub>2</sub>O<sub>5</sub> at higher temperatures, transitioning around 1360°C.<sup>13-25</sup> Recent studies have successfully elucidated the atomic structure of L-Ta<sub>2</sub>O<sub>5</sub>, known as the  $\lambda$  model.<sup>26</sup> However, the detailed atomic configuration of H-Ta<sub>2</sub>O<sub>5</sub> remains a long-standing and unresolved challenge despite extensive investigation.

The H-Ta<sub>2</sub>O<sub>5</sub> phase can be stabilized at lower temperatures through rapid quenching or the introduction of small quantities of impurity ions. This phase typically manifests in a tetragonal<sup>13-19</sup> or pseudo-tetragonal<sup>17-25</sup> crystal system, with both structures exhibiting similar lattice constants ( $a \approx b \approx 3.8 \text{ \AA}$  and  $c \approx 36 \text{ \AA}$ ). Temperature-dependent studies have shown that pseudo-tetragonal structures with underlying orthorhombic, monoclinic, or triclinic symmetries transform into a tetragonal form upon heating,<sup>17-19</sup> suggesting that the tetragonal structure is the intrinsic arrangement of atoms in H-Ta<sub>2</sub>O<sub>5</sub>. High-resolution electron microscopy (HREM) has confirmed an  $I4_1/amd$  space group for the Ta sublattice,<sup>15</sup> but the precise configuration of the O sublattice remains unknown. Density functional theory (DFT) calculations combined with evolutionary search algorithms have proposed a tetragonal model with  $I4_1/amd$  symmetry as the energetically favored configuration.<sup>27,28</sup> However, a significant discrepancy between the theoretically predicted  $c$  lattice constant (26.3  $\text{\AA}$ ) and the experimentally observed value ( $\approx 36 \text{ \AA}$ ) highlights the challenges in definitively determining the atomic structure of H-Ta<sub>2</sub>O<sub>5</sub>.

In this study, we successfully determined the atomic structure of H-Ta<sub>2</sub>O<sub>5</sub> and discovered a

remarkable phenomenon of collective oxygen transport within its crystalline lattice. Using DFT calculations, we revealed that H-Ta<sub>2</sub>O<sub>5</sub> adopts a chiral tetragonal structure, constructed from orthorhombic  $\lambda$  units characteristic of L-Ta<sub>2</sub>O<sub>5</sub>, resulting in a large 168-atom unit cell. Ab-initio molecular dynamics simulations demonstrated that a subset of oxygen atoms in this structure exhibits a cooperative drift through single-atom-width channels within the solid crystalline framework. This collective motion has a remarkably low energy barrier of only 0.2 eV, enabling it to occur even at temperatures as low as a few hundred degrees Celsius. The flexible octahedral coordination environment at the screw-rotation planes is identified as the key factor driving the exceptional mobility of oxygen ions, facilitating extensive structural relaxation and dynamic charge rebalancing during oxygen transport. Finally, we provide evidence from existing experimental observations that supports this significant atomic transport mechanism.

## RESULTS

### Crystal structure of tetragonal Ta<sub>2</sub>O<sub>5</sub>

The orthorhombic- $\lambda$  structure<sup>26</sup> of L-Ta<sub>2</sub>O<sub>5</sub> is crucial for understanding our findings on H-Ta<sub>2</sub>O<sub>5</sub>. It is characterized by two-dimensional Ta<sub>2</sub>O<sub>3</sub> layers stacked along the  $c$ -axis and linked by oxygen atoms (Fig. 1a). Within each Ta<sub>2</sub>O<sub>3</sub> layer, all Ta atoms share a uniform coordination environment, each bonded to three O atoms with three bonds and one O atom with two bonds (Fig. 1b). Molecular dynamics simulations show that, at finite temperatures, the Ta atoms in the Ta<sub>2</sub>O<sub>3</sub> layer form a distinct triangular lattice (Fig. 1c), consistent with the triangular Ta sublattice observed in X-ray diffraction (XRD) studies.<sup>29</sup> This result allows the adaptation of the orthorhombic- $\lambda$  model onto a triangular grid (Fig. 1d), where the twofold-coordinated O atoms, characterized by substantial transverse vibration amplitude, are depicted as connecting lines between the grid points.

Our “tetragonal- $\lambda$ ” structure for H-Ta<sub>2</sub>O<sub>5</sub> is based on HREM images.<sup>15</sup> These images reveal a tetragonal Ta sublattice with  $I4_1/amd$  symmetry, characterized by fourfold screw symmetry (Fig. 1e). The repeating unit of the Ta sublattice, located between 90° rotation planes, consists of stacked layers of triangular Ta lattices, similar to the arrangement found in the orthorhombic- $\lambda$  structure. We constructed our tetragonal model for H-Ta<sub>2</sub>O<sub>5</sub> by incorporating the orthorhombic- $\lambda$  structure into the tetragonal framework with 4<sub>1</sub> screw symmetry (see Supplementary Note 1 for details). The resulting pre-relaxation structure, shown in Fig. 1f, belongs to the chiral space group

$P4_12_12$  (No. 92) and displays right-handed screw symmetry. Its unit cell has a lateral lattice constant twice that reported in the HREM study and contains 24  $\text{Ta}_2\text{O}_5$  formula units (168 atoms). An energetically equivalent left-handed enantiomorph exists, belonging to the space group  $P4_32_12$  (No. 96) (Supplementary Note 2 and Supplementary Fig. 1). For simplicity, we will focus on the right-handed structure in the following discussion.

Structural relaxation of the tetragonal- $\lambda$  model using DFT calculations (see Methods for calculation details) preserved its space group symmetry and revealed the complete atomic structure of H- $\text{Ta}_2\text{O}_5$  (Fig. 1g; see Supplementary Information for structural data in CIF format). The relaxation process significantly altered the local coordination of Ta atoms at the screw-rotation planes, where two orthorhombic- $\lambda$  blocks are connected by a  $90^\circ$  twist. These Ta atoms adopt octahedral coordination with a slight distortion, where of the four horizontally bonded oxygen atoms, two are positioned slightly above and two slightly below the equatorial plane (Fig. 1i). This contrasts with the Ta atoms away from the screw-rotation planes, which retain the pentagonal bipyramidal or distorted octahedral coordination inherited from the  $\lambda$  structure. Our calculations showed that the tetragonal- $\lambda$  phase is energetically more favorable than the orthorhombic- $\lambda$  phase by 0.10 eV per formula unit (Supplementary Note 3 and Supplementary Table 1). The relaxed lattice constants are  $a = b = 7.6 \text{ \AA}$  and  $c = 35.8 \text{ \AA}$ , showing excellent agreement with experimental values.

A key assumption in the tetragonal- $\lambda$  model is that the number of Ta rows between screw-rotation planes ( $N_{\text{Ta}}$ ) is 3, which aligns with the HREM images (Fig. 1e). This  $N_{\text{Ta}}$  value is a defining structural characteristic of H- $\text{Ta}_2\text{O}_5$ . To validate that the tetragonal- $\lambda$  model accurately reproduces the periodicity along the [001] direction, we investigated models with  $N_{\text{Ta}}$  values ranging from 2 to 6 (Supplementary Fig. 2). We calculated the screw-rotation energy ( $E_{\text{SR}}$ ), which quantifies the energy cost associated with introducing screw-rotation planes into the orthorhombic- $\lambda$  structure to form the tetragonal- $\lambda$  structure (see Methods for details). Notably,  $E_{\text{SR}}$  is negative only when  $N_{\text{Ta}} = 3$  (Fig. 1h and Supplementary Table 2), indicating that the incorporation of screw-rotation planes is energetically favorable only in this case. For other  $N_{\text{Ta}}$  values,  $E_{\text{SR}}$  is positive, suggesting an energetic penalty for such incorporation. Relaxed atomic structures with  $N_{\text{Ta}} \neq 3$  show considerable structural distortions (Supplementary Fig. 2), likely attributable to strain induced by the screw-rotation planes. These findings strongly support the tetragonal- $\lambda$  model with  $N_{\text{Ta}} = 3$  as the definitive structure of H- $\text{Ta}_2\text{O}_5$ .

Density of states (DOS) calculations for the tetragonal- $\lambda$  phase predict a band gap of 2.4 eV, slightly larger than the 2.2 eV band gap calculated for the orthorhombic- $\lambda$  phase (Supplementary

Fig. 3). The close similarity in band gaps suggests that the tetragonal- $\lambda$  phase maintains the correct formal oxidation states of +5 for Ta and -2 for O, akin to the orthorhombic- $\lambda$  phase<sup>26</sup> (Supplementary Note 4). This result implies a high degree of stability in the electronic structure of the tetragonal- $\lambda$  phase. Previous studies using hybrid functional calculations, which correct the band gap underestimation inherent in the standard GGA method (also used in this work), have reported a band gap value of around 4.0 eV for the orthorhombic- $\lambda$  phase,<sup>26,28,30</sup> consistent with the experimental value of 3.9 eV for L-Ta<sub>2</sub>O<sub>5</sub>.<sup>31</sup> Although experimental data for H-Ta<sub>2</sub>O<sub>5</sub> are currently unavailable, we anticipate a similar band gap for the tetragonal- $\lambda$  phase.

### **Dynamical behavior of tetragonal Ta<sub>2</sub>O<sub>5</sub>**

HREM revealed an achiral structure (space group  $I4_1/amd$ ) for the Ta sublattice in H-Ta<sub>2</sub>O<sub>5</sub>.<sup>15</sup> However, the tetragonal- $\lambda$  model predicts chiral structures with a doubled lateral lattice constant. To reconcile this discrepancy, we performed ab-initio molecular dynamics simulations (see Methods). Fig. 2a,b show the trajectories of Ta atoms simulated at 1000 K over 5 picoseconds, projected along the [010] and  $[\bar{1}10]$  axes, respectively. Figure 2a demonstrates that over time, the Ta atoms within each Ta<sub>2</sub>O<sub>3</sub> layer dynamically arrange into a well-defined triangular lattice. This thermally averaged Ta sublattice, with a lattice constant half that of the tetragonal- $\lambda$  model, matches the HREM image perfectly. Fig. 2b further confirms that the tetragonal- $\lambda$  model accurately reflects the HREM images obtained for H-Ta<sub>2</sub>O<sub>5</sub>.

The trajectories of oxygen atoms from the molecular dynamics simulations uncover unexpected ionic transport channels within the crystal structure. While most oxygen atoms vibrate near their equilibrium positions, those situated midway between screw-rotation planes exhibit anomalous behavior, characterized by continuous, wavy trajectories that overlap with one another (Fig. 2c). Further investigation into individual atomic movements (Supplementary Video 1 and Fig. 2d) reveals a collective drift of oxygen atoms along the [100] or [010] directions within their respective Ta<sub>2</sub>O<sub>3</sub> layers. Fig. 2e tracks three consecutive oxygen atoms in the same layer moving along the [100] direction, showing that they move in sync, maintaining nearly constant interatomic distances. This concerted floating motion, occurring independently across various Ta<sub>2</sub>O<sub>3</sub> layers, involves dynamic shifts between twofold and threefold bonding configurations of the drifting oxygen atoms as they adapt to their local environments (Fig. 2d). Simulations show that the drift persists down to 500 K (Supplementary Fig. 4). Interestingly, in the orthorhombic- $\lambda$  structure, atoms sharing

similar local bonding configurations (Fig. 1b) do not show such collective transport, even at elevated temperatures of 1500 K (Supplementary Fig. 5). This stark contrast highlights the unique dynamic properties of oxygen atoms in the tetragonal- $\lambda$  structure.

To investigate the mechanism behind cooperative ionic movement in the tetragonal- $\lambda$  structure, we analyzed its energy barrier and transition states using the nudged elastic band method (see Methods for details). For comparison, we also evaluated the orthorhombic- $\lambda$  structure. The results reveal a substantially lower energy barrier in the tetragonal- $\lambda$  structure (0.21 eV) compared to the orthorhombic- $\lambda$  structure (1.8 eV) (Fig. 3a), with the latter serving as a representative model of typical crystalline materials. This difference arises from contrasting levels of atomic flexibility at their respective transition states.

In the orthorhombic- $\lambda$  structure, limited atomic flexibility leads to significant bond distortion around the two tantalum atoms (Ta1 and Ta2) bonded to the migrating oxygen atoms (Fig. 3c). This distortion, arising from the restricted coordination environment of neighboring oxygen atoms, results in an imbalance in formal oxidation states. Calculations indicate that these Ta atoms gain an additional 0.47 electrons at the transition state (Fig. 4a), destabilizing the electronic structure. In contrast, the tetragonal- $\lambda$  structure permits greater adaptability, featuring two-step transition states separated by a gentle energy ridge, where bond distortions from oxygen migration are effectively mitigated by flexible bonding with nearby oxygen atoms (O1-O4) (Fig. 3e). These oxygen atoms, which connect the Ta atoms horizontally within the octahedral arrangement at the screw-rotation planes, can adjust their vertical positions (Fig. 1i and Supplementary Video 1). This adaptable oxygen coordination keeps changes in local atomic charges of Ta atoms below 0.1 electrons (Fig. 4b), thereby stabilizing the transition state and contributing the overall dynamic stability of the tetragonal- $\lambda$  structure.

Our detailed analysis of atomic displacements between the initial and transition states further reveals a pronounced reorganization, particularly within the oxygen sublattice (Fig. 5a). The relaxation of the O1-O4 oxygen atoms triggers a cascading rearrangement across the lattice, causing substantial positional shifts in atoms up to 9 Å away (spanning six interatomic bonds). It also leads to notable out-of-plane displacements of distant oxygen atoms (Fig. 5b). This extensive network of atomic adjustments effectively dissipates local strain and mitigates charge imbalances arising from the migration of mobile oxygen atoms. In the orthorhombic- $\lambda$  structure, however, atomic movement is more limited, primarily confined to second-nearest-neighbor oxygen atoms within the same Ta<sub>2</sub>O<sub>3</sub> layer (Fig. 5c,d). This constrained motion, markedly different from the extensive

atomic rearrangement in the tetragonal- $\lambda$  structure, underscores the essential role of the flexible Ta-O octahedral coordination environment at the screw-rotation planes. This unique feature of the tetragonal- $\lambda$  phase enables efficient dissipation of stress and charge imbalances, facilitating collective atomic displacement throughout the crystal lattice.

## DISCUSSION

The discovery of mobile oxygen atoms within the H-Ta<sub>2</sub>O<sub>5</sub> structure offers new insights into several previously unexplained phenomena. Firstly, it helps to explain the distinct stabilities of H-Ta<sub>2</sub>O<sub>5</sub> and L-Ta<sub>2</sub>O<sub>5</sub> under vacuum conditions. Above the phase transition temperature, H-Ta<sub>2</sub>O<sub>5</sub> remains stable in oxygen-rich environments but decomposes under vacuum, releasing oxygen gas and tantalum metal.<sup>20,32</sup> In contrast, L-Ta<sub>2</sub>O<sub>5</sub> demonstrates stability in hydrogen at 1250°C.<sup>20</sup> This difference is consistent with the presence of a collective ionic transport channel in the tetragonal- $\lambda$  phase of H-Ta<sub>2</sub>O<sub>5</sub>, contrasting with the more rigid lattice structure of the orthorhombic- $\lambda$  phase in L-Ta<sub>2</sub>O<sub>5</sub>.

Secondly, this finding sheds light on the exceptionally high oxygen ion conductivity observed in H-Ta<sub>2</sub>O<sub>5</sub>, which exceeds that of L-Ta<sub>2</sub>O<sub>5</sub> by orders of magnitude.<sup>33–36</sup> This enhanced conductivity has been found to be intrinsic to H-Ta<sub>2</sub>O<sub>5</sub>, remaining largely independent of dopant type, concentration, and oxygen pressure once above a certain threshold.<sup>35,36</sup> This behavior aligns well with the collective oxygen transport mechanism identified in our study. Moreover, the pronounced anisotropy in conductivity—where the [100] direction exhibits conductivity two orders of magnitude higher than the [001] direction<sup>35,36</sup>—further supports our findings regarding the existence of a collective oxygen transport channel within the tetragonal- $\lambda$  structure.

In conclusion, our research successfully addresses the long-standing challenge of determining the crystalline structure of H-Ta<sub>2</sub>O<sub>5</sub>. Crucially, we have identified a collective oxygen transport channel within this material, enabling defect-free oxygen mobility at relatively low temperatures (above a few hundred degrees Celsius). This mobility is facilitated by the flexible coordination environment at the screw-rotation planes, which allows extensive structural relaxation and dynamic charge rebalancing, thereby lowering the energy barrier for atomic movement. This finding provides a comprehensive explanation for previously observed behaviors of H-Ta<sub>2</sub>O<sub>5</sub>, particularly its instability under vacuum and its anisotropic high oxygen ion conductivity.

The insights gained from this study provide valuable guidance for designing materials with

enhanced atomic mobility, which is essential for applications such as neuromorphic devices, fuel cells, and batteries. Additionally, they hold promise for developing materials with low-barrier ionic motion, potentially benefiting ferroelectrics and high-k dielectrics in electronic devices. Although translating these insights into practical material design poses challenges, the rapid advancements in artificial intelligence-powered materials discovery platforms<sup>37,38</sup> could enable the integration of flexible structural units within crystalline frameworks, paving the way for novel functional materials previously unimagined.

## METHODS

### Density functional theory calculations

Our DFT studies were performed using the Vienna Ab Initio Simulation Package (VASP).<sup>39,40</sup> We utilized the projector augmented wave (PAW) method<sup>41</sup> and employed the generalized gradient approximation (GGA) for the exchange-correlation potential, specifically adopting the version refined for solids and surfaces (PBEsol).<sup>42</sup> The electronic wave functions were represented using a plane-wave basis set with cutoff energies set at 500 eV for structural optimizations and 400 eV for molecular dynamics simulations. For the integration over reciprocal space, we used a  $4 \times 4 \times 1$  k-point mesh within the Brillouin zone of the tetragonal- $\lambda$  structure and equivalent-density meshes for other structures studied. The lattice constants and atomic positions for each structure were optimized using the variable cell optimization method in VASP, with all atoms relaxed until the forces on them were less than  $0.01 \text{ eV/\AA}$ . Ab-initio molecular dynamics simulations of the canonical ensemble (NVT conditions) were performed using the Nosé thermostat, as implemented in VASP.<sup>43,44</sup> The Nosé mass parameter was set to produce a temperature fluctuation period of around 80 picoseconds. Atomic structures are visualized using VESTA.<sup>45</sup>

### Screw-rotation energy

To quantify the energetic cost of introducing screw-rotation planes into the orthorhombic- $\lambda$  structure, thereby transforming it into the tetragonal- $\lambda$  structure, we define the screw-rotation energy ( $E_{\text{SR}}$ ) using the following equation:

$$E_{\text{SR}} = \frac{1}{4} \left( E_{\text{tot}}^{\text{tetra}} - \frac{N_{\text{f.u.}}^{\text{tetra}}}{N_{\text{f.u.}}^{\text{ortho}}} E_{\text{tot}}^{\text{ortho}} \right).$$

Here,  $E_{\text{tot}}^{\text{tetra}}$  and  $E_{\text{tot}}^{\text{ortho}}$  represent the total energies per unit cell of the tetragonal- $\lambda$  and orthorhombic- $\lambda$  structures, respectively, while  $N_{\text{f.u.}}^{\text{tetra}}$  and  $N_{\text{f.u.}}^{\text{ortho}}$  are the numbers of  $\text{Ta}_2\text{O}_5$  formula units in each respective unit cell. The factor of  $1/4$  arises because the tetragonal- $\lambda$  unit cell contains four screw-rotation planes. For a total energy difference of  $-0.10 \text{ eV}$  per formula unit at  $N_{\text{Ta}} = 3$ , this corresponds to an energy per screw-rotation plane of  $E_{\text{SR}} = -0.59 \text{ eV}$  (Fig. 1h and Supplementary Table 2). The negative sign indicates the energetic preference for the tetragonal- $\lambda$  structure, or equivalently, the preference for incorporating the screw-rotation plane.

## Nudged elastic band calculations

The energy barriers for collective atomic displacements were determined using the nudged elastic band (NEB) method, which incorporates the climbing image technique and an improved tangent estimation method to enhance accuracy.<sup>46,47</sup> To ensure consistency in the calculated energy barriers and transition states, we employed a range of 4 to 6 NEB images between the initial and final structures. For the tetragonal- $\lambda$  structure, we employed the unit cell with dimensions of  $7.72 \text{ \AA} \times 7.72 \text{ \AA} \times 36.18 \text{ \AA}$  to examine the collective ionic transport along the [100] direction in one of the  $\text{Ta}_2\text{O}_3$  layers. The unit cell contains two inequivalent  $\text{Ta}_2\text{O}_3$  layers, and the calculations showed nearly identical energy barriers for these layers, differing by only 0.01 eV. For the orthorhombic- $\lambda$  structure, the NEB calculations were performed using a supercell comprising two  $\text{Ta}_2\text{O}_3$  layers, each with an area of  $7.33 \text{ \AA} \times 24.77 \text{ \AA}$ , corresponding to a  $(1 \times 4)$  supercell in the  $\text{Ta}_2\text{O}_3$  layer. In these calculations, the oxygen atoms were displaced along the short axis in one of the  $\text{Ta}_2\text{O}_3$  layers.

- 
- [1] G. C. Farrington and J. L. Briant, Fast ionic transport in solids, *Science* **204**, 1371 (1979).
- [2] P. Knauth and H. L. Tuller, Solid-state ionics: Roots, status, and future prospects, *J. Am. Ceram. Soc.* **85**, 1654 (2002).
- [3] H. Tuller, Ionic conduction and applications, in *Springer Handbook of Electronic and Photonic Materials*, edited by S. Kasap and P. Capper (Springer International Publishing, Cham, 2017) Chap. 11, pp. 247–266.
- [4] G. L. Brennecka and D. A. Payne, Preparation of dense Ta<sub>2</sub>O<sub>5</sub>-based ceramics by a coated powder method for enhanced dielectric properties, *J. Am. Ceram. Soc.* **89**, 2089 (2006).
- [5] J. Robertson and R. M. Wallace, High-K materials and metal gates for CMOS applications, *Mater. Sci. Eng. R Rep.* **88**, 1 (2015).
- [6] B. Wang, W. Huang, L. Chi, M. Al-Hashimi, T. J. Marks, and A. Facchetti, High-*k* gate dielectrics for emerging flexible and stretchable electronics, *Chem. Rev.* **118**, 5690 (2018).
- [7] M.-J. Lee, C. B. Lee, D. Lee, S. R. Lee, M. Chang, J. H. Hur, Y.-B. Kim, C.-J. Kim, D. H. Seo, S. Seo, U.-I. Chung, I.-K. Yoo, and K. Kim, A fast, high-endurance and scalable non-volatile memory device made from asymmetric Ta<sub>2</sub>O<sub>5-*x*</sub>/TaO<sub>2-*x*</sub> bilayer structures, *Nat. Mater.* **10**, 625 (2011).
- [8] T. Kim, H. Son, I. Kim, J. Kim, S. Lee, J. K. Park, J. Y. Kwak, J. Park, and Y. Jeong, Reversible switching mode change in Ta<sub>2</sub>O<sub>5</sub>-based resistive switching memory (ReRAM), *Sci. Rep.* **10**, 11247 (2020).
- [9] W. Wang, F. Yin, H. Niu, Y. Li, E. S. Kim, and N. Y. Kim, Tantalum pentoxide (Ta<sub>2</sub>O<sub>5</sub> and Ta<sub>2</sub>O<sub>5-*x*</sub>)-based memristor for photonic in-memory computing application, *Nano Energy* **106**, 108072 (2023).
- [10] V. Gurylev, A review on the development and advancement of Ta<sub>2</sub>O<sub>5</sub> as a promising photocatalyst, *Mater. Today Sustain.* **18**, 100131 (2022).
- [11] Y. R. Zheng, J. Vernieres, Z. Wang, K. Zhang, D. Hochfilzer, K. Krempf, T. W. Liao, F. Presel, T. Altantzis, J. Fatermans, S. B. Scott, N. M. Secher, C. Moon, P. Liu, S. Bals, S. Van Aert, A. Cao, M. Anand, J. K. Nørskov, J. Kibsgaard, and I. Chorkendorff, Monitoring oxygen production on mass-selected iridium–tantalum oxide electrocatalysts, *Nat. Energy* **7**, 55 (2022).
- [12] T. Sertel, N. A. Sonmez, S. S. Cetin, and S. Ozcelik, Influences of annealing temperature on anti-reflective performance of amorphous Ta<sub>2</sub>O<sub>5</sub> thin films, *Ceram. Int.* **45**, 11 (2019).

- [13] A. I. Zaslavskii, R. A. Zvinchuk, and A. G. Tutov, X-ray studies of Ta<sub>2</sub>O<sub>5</sub> polymorphism, *Dokl. Akad. Nauk SSSR* **104**, 409 (1955).
- [14] R. S. Roth, J. L. Waring, and W. S. Brower, Effect of oxide additions on the polymorphism of tantalum pentoxide: II. “Stabilization” of the high temperature structure type, *J. Res. Natl. Bur. Stand. A Phys. Chem.* **74A**, 477–484 (1970).
- [15] X. Q. Liu, X. D. Han, Z. Zhang, L. F. Ji, and Y. J. Jiang, The crystal structure of high temperature phase Ta<sub>2</sub>O<sub>5</sub>, *Acta Mater.* **55**, 2385 (2007).
- [16] N. Terao, Structure des oxides de tantale, *Jpn. J. Appl. Phys.* **6**, 21 (1967).
- [17] F. Laves and W. Petter, Eine displazive umwandlung bei  $\alpha$ -Ta<sub>2</sub>O<sub>5</sub>, *Helv. Phys. Acta* **37**, 617 (1964).
- [18] J. L. Waring and R. S. Roth, Effect of oxide additions on polymorphism of tantalum pentoxide (system Ta<sub>2</sub>O<sub>5</sub>-TiO<sub>2</sub>), *J. Res. Natl. Bur. Stand. A Phys. Chem.* **72A**, 175 (1968).
- [19] V. V. Plies and R. Gruehn, Zum thermischen verhalten metastabiler H-Ta<sub>2</sub>O<sub>5</sub>-varianten im system Ta<sub>2</sub>O<sub>5</sub>-TiO<sub>2</sub>, *Z. Anorg. Allg. Chem.* **463**, 32 (1980).
- [20] S. Lagergren and A. Magnéli, On the tantalum-oxygen system, *Acta Chem. Scand.* **6**, 444 (1952), and ASTM Card 5-0258.
- [21] A. Reisman, F. Holtzberg, M. Berkenblit, and M. Berry, Reactions of the group VB pentoxides with alkali oxides and carbonates. III. thermal and X-ray phase diagrams of the system K<sub>2</sub>O or K<sub>2</sub>CO<sub>3</sub> with Ta<sub>2</sub>O<sub>5</sub>, *J. Am. Chem. Soc.* **78**, 4514 (1956).
- [22] N. Stephenson and R. Roth, The crystal structure of the high temperature form of Ta<sub>2</sub>O<sub>5</sub>, *J. Solid State Chem.* **3**, 145 (1971).
- [23] D. Makovec, J.-M. Zuo, R. Twisten, and D. A. Payne, A high-temperature structure for Ta<sub>2</sub>O<sub>5</sub> with modulations by TiO<sub>2</sub> substitution, *J. Solid State Chem.* **179**, 1782 (2006).
- [24] W. Mertin, R. Gruehn, and H. Schäfer, Neue beobachtungen zum system TiO<sub>2</sub>-Ta<sub>2</sub>O<sub>5</sub>, *J. Solid State Chem.* **1**, 425 (1970).
- [25] G. L. Brennecka, D. A. Payne, P. Sarin, J.-M. Zuo, W. M. Kriven, and H. Hellwig, Phase transformations in the high-temperature form of pure and TiO<sub>2</sub>-stabilized Ta<sub>2</sub>O<sub>5</sub>, *J. Am. Ceram. Soc.* **90**, 2947 (2007).
- [26] S.-H. Lee, J. Kim, S.-J. Kim, S. Kim, and G.-S. Park, Hidden structural order in orthorhombic Ta<sub>2</sub>O<sub>5</sub>, *Phys. Rev. Lett.* **110**, 235502 (2013).
- [27] Y. Yang and Y. Kawazoe, Prediction of new ground-state crystal structure of Ta<sub>2</sub>O<sub>5</sub>, *Phys. Rev. Mater.* **2**, 034602 (2018).

- [28] J.-H. Yuan, K.-H. Xue, Q. Chen, L. R. C. Fonseca, and X.-S. Miao, Ab initio simulation of Ta<sub>2</sub>O<sub>5</sub>: A high symmetry ground state phase with application to interface calculation, *Ann. Phys.* **531**, 1800524 (2019).
- [29] K. Lehovc, Lattice structure of  $\beta$ -Ta<sub>2</sub>O<sub>5</sub>, *J. Less Common Met.* **7**, 397 (1964).
- [30] Y. Guo and J. Robertson, Oxygen vacancy defects in Ta<sub>2</sub>O<sub>5</sub> showing long-range atomic rearrangements, *Appl. Phys. Lett.* **104**, 112906 (2014).
- [31] W. J. Chun, A. Ishikawa, H. Fujisawa, T. Takata, J. N. Kondo, M. Hara, M. Kawai, Y. Matsumoto, and K. Domen, Conduction and valence band positions of Ta<sub>2</sub>O<sub>5</sub>, TaON, and Ta<sub>3</sub>N<sub>5</sub> by UPS and electrochemical methods, *J. Phys. Chem. B* **107**, 1798 (2003).
- [32] W. von Bolton, Das tantal, seine darstellung und seine eigenschaften, *Z. Elektrochem.* **11**, 45 (1905).
- [33] A. E. McHale and H. L. Tuller, New tantalum-based solid oxide electrolytes, *Solid State Ionics* **5**, 515 (1981).
- [34] A. E. McHale and H. L. Tuller, Defects and charge transport in stabilized  $\alpha$ -Ta<sub>2</sub>O<sub>5</sub>, *Radia. Eff.* **75**, 267 (1983).
- [35] G. M. Choi, H. L. Tuller, and J. S. Haggerty, Alpha-Ta<sub>2</sub>O<sub>5</sub>: An intrinsic fast oxygen ion conductor, *J. Electrochem. Soc.* **136**, 835 (1989).
- [36] G. M. Choi and H. L. Tuller, Nonstoichiometry and mixed conduction in  $\alpha$ -Ta<sub>2</sub>O<sub>5</sub>, *J. Am. Ceram. Soc.* **73**, 1700 (1990).
- [37] A. Merchant, S. Batzner, S. S. Schoenholz, M. Aykol, G. Cheon, and E. D. Cubuk, Scaling deep learning for materials discovery, *Nature* **624**, 80 (2023).
- [38] N. J. Szymanski, B. Rendy, Y. Fei, R. E. Kumar, T. He, D. Milsted, M. J. McDermott, M. Gallant, E. D. Cubuk, A. Merchant, H. Kim, A. Jain, C. J. Bartel, K. Persson, Y. Zeng, and G. Ceder, An autonomous laboratory for the accelerated synthesis of novel materials, *Nature* **624**, 86 (2023).
- [39] G. Kresse and J. Furthmüller, Efficient iterative schemes for ab initio total-energy calculations using a plane-wave basis set, *Phys. Rev. B* **54**, 11169 (1996).
- [40] G. Kresse and D. Joubert, From ultrasoft pseudopotentials to the projector augmented-wave method, *Phys. Rev. B* **59**, 1758 (1999).
- [41] P. E. Blöchl, Projector augmented-wave method, *Phys. Rev. B* **50**, 17953 (1994).
- [42] J. P. Perdew, A. Ruzsinszky, G. I. Csonka, O. A. Vydrov, G. E. Scuseria, L. A. Constantin, X. Zhou, and K. Burke, Restoring the density-gradient expansion for exchange in solids and surfaces, *Phys. Rev. Lett.* **100**, 136406 (2008).

- [43] S. Nosé, Constant temperature molecular dynamics methods, [Prog. Theor. Phys. Supp. \*\*103\*\*, 1 \(1991\)](#).
- [44] D. M. Bylander and L. Kleinman, Energy fluctuations induced by the nosé thermostat, [Phys. Rev. B \*\*46\*\*, 13756 \(1992\)](#).
- [45] K. Momma and F. Izumi, *VESTA3* for three-dimensional visualization of crystal, volumetric and morphology data, [J. Appl. Cryst. \*\*44\*\*, 1272 \(2011\)](#).
- [46] G. Henkelman, B. P. Uberuaga, and H. Jónsson, A climbing image nudged elastic band method for finding saddle points and minimum energy paths, [J. Chem. Phys. \*\*113\*\*, 9901 \(2000\)](#).
- [47] G. Henkelman and H. Jónsson, Improved tangent estimate in the nudged elastic band method for finding minimum energy paths and saddle points, [J. Chem. Phys. \*\*113\*\*, 9978 \(2000\)](#).

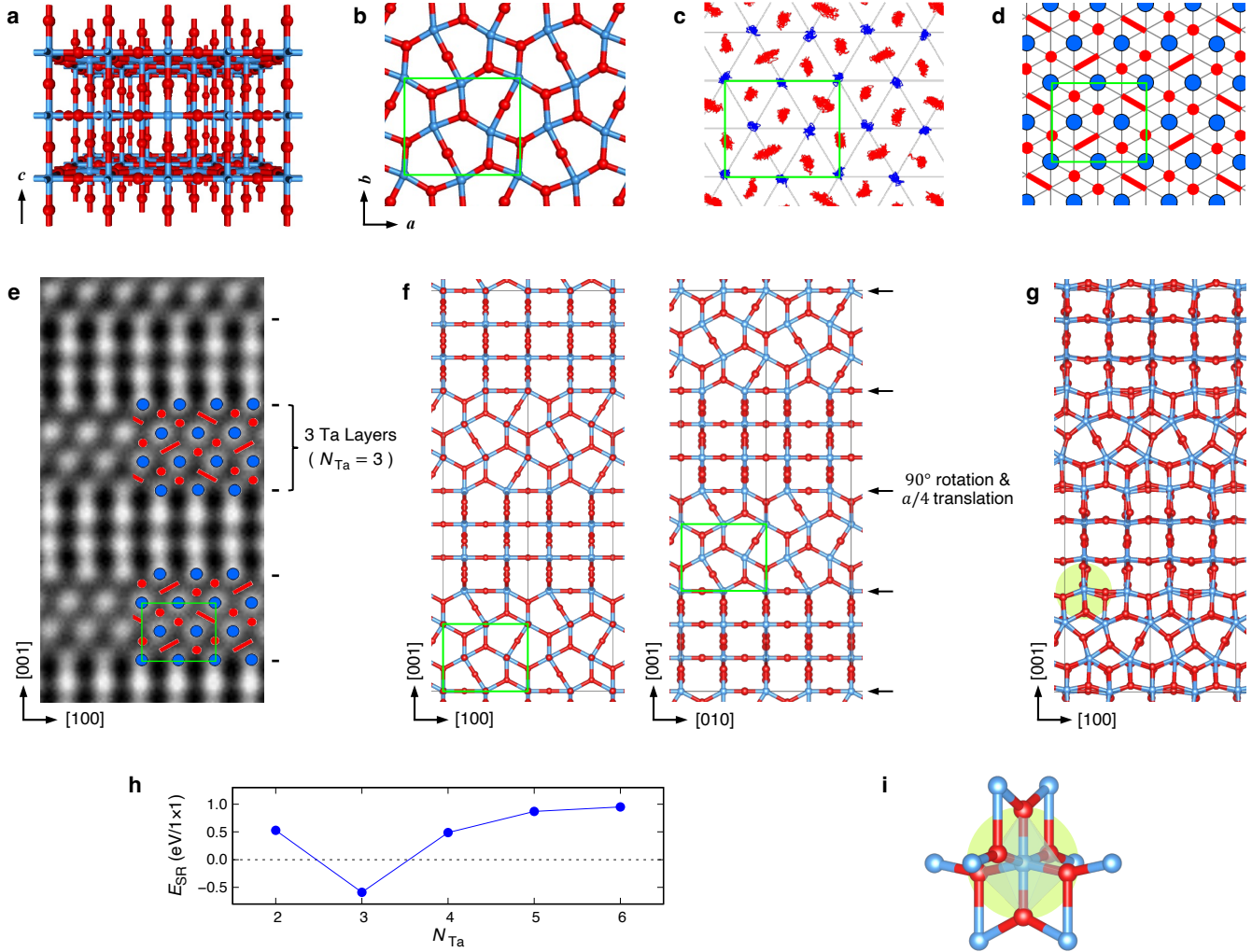


**FIG. 1. Orthorhombic- $\lambda$  structure of L-Ta<sub>2</sub>O<sub>5</sub> vs. tetragonal- $\lambda$  structure of H-Ta<sub>2</sub>O<sub>5</sub>.** **a-d** Orthorhombic- $\lambda$  structure of L-Ta<sub>2</sub>O<sub>5</sub>. **a** Perspective view, with blue and red spheres representing Ta and O atoms, respectively. **b** Detailed view of the  $\lambda$  structure within the Ta<sub>2</sub>O<sub>3</sub> layer, with the 2D unit cell outlined in green. **c** Atomic trajectories within the Ta<sub>2</sub>O<sub>3</sub> plane during a constant-volume molecular dynamics simulation at 1000 K. **d** Representation of the  $\lambda$  model using a triangular grid. **e-i** Tetragonal- $\lambda$  structure of H-Ta<sub>2</sub>O<sub>5</sub>. **e** High-resolution electron microscopy (HREM) image<sup>15</sup> overlaid with the triangular-grid  $\lambda$  model.  $N_{\text{Ta}}$  represents the number of Ta rows between 90° rotation planes. **f** Initial (pre-relaxation) atomic structure of the tetragonal- $\lambda$  model with  $4_1$  screw symmetry, shown in two projections, with black arrows indicating screw-rotation planes. **g** Relaxed atomic structure of the model shown in (f). **h** Screw-rotation energy ( $E_{\text{SR}}$ ) as a function of  $N_{\text{Ta}}$ .  $E_{\text{SR}}$  measures the energy cost of incorporating screw-rotation planes into the orthorhombic- $\lambda$  structure to form the tetragonal- $\lambda$  structure (see Methods). (1 × 1) indicates the lateral area of the unit cell. **i** Schematic representation of the distorted octahedral coordination of Ta atoms at the screw-rotation planes.

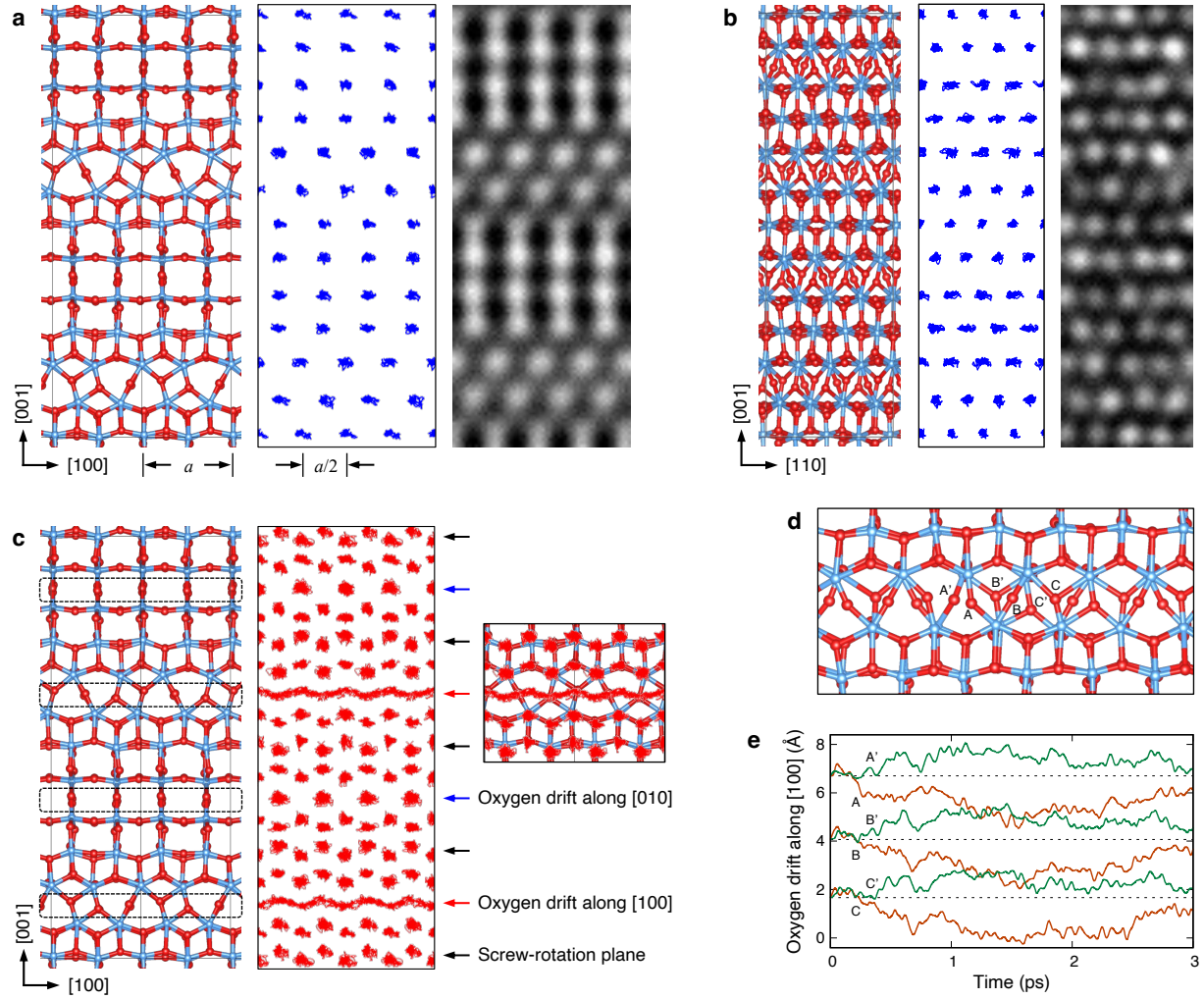


FIG. 2. **Ab-initio molecular dynamics simulations of the tetragonal- $\lambda$  structure.** **a** Trajectories of Ta atoms at 1000 K over 5 picoseconds (ps), viewed along the [010] direction, alongside the corresponding high-resolution electron microscopy (HREM) image.<sup>15</sup> **b** Trajectories of the same Ta atoms viewed along the  $[\bar{1}10]$  direction, with the associated HREM image.<sup>15</sup> **c** Trajectories of O atoms in the same simulation, where drifting O atoms display continuous, wavy paths. The panel on the right illustrates the oxygen trajectories overlaid on the atomic structure. **d** Snapshot of the simulations, showing two layers of Ta<sub>2</sub>O<sub>3</sub>. **e** Positions of three consecutive O atoms on the same Ta<sub>2</sub>O<sub>3</sub> layer under collective drift. Two sets in adjacent Ta<sub>2</sub>O<sub>3</sub> layers are shown in different colors.

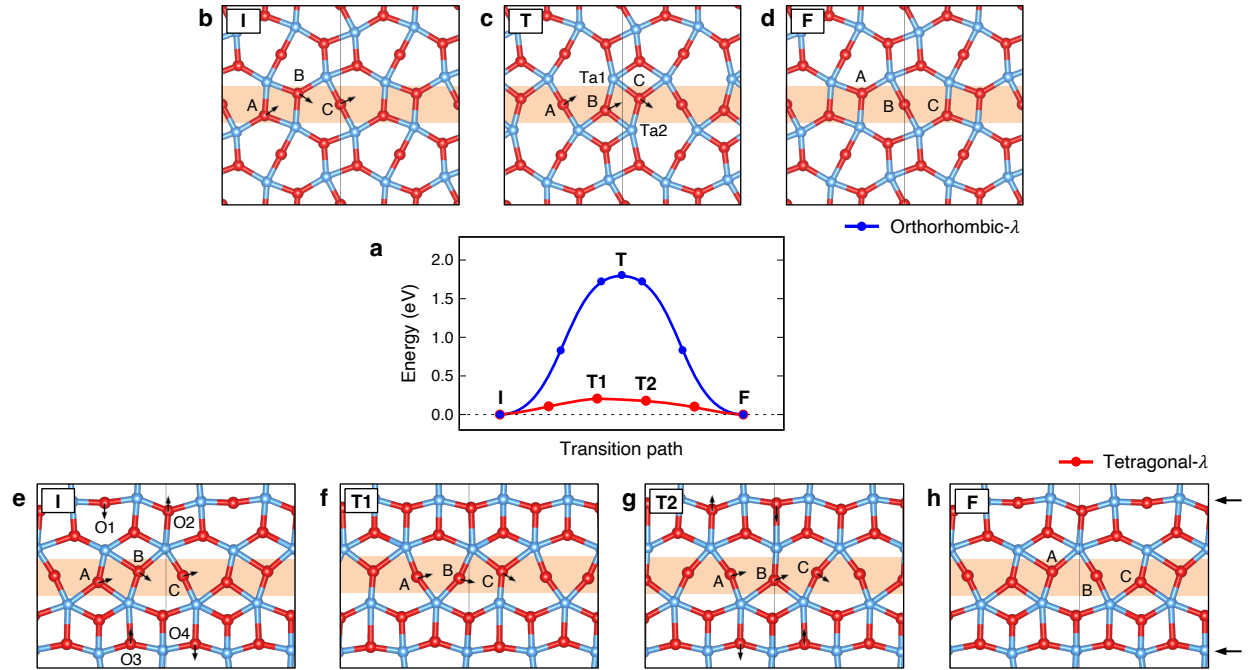


FIG. 3. **Energy barrier and transition state for collective oxygen transport.** **a** Energy diagram for collective oxygen drift calculated using the nudged elastic band (NEB) method, comparing results for the tetragonal- $\lambda$  and orthorhombic- $\lambda$  structures. **b-h** Atomic structures for the initial (I), transition (T), and final (F) states along the drift pathway for the orthorhombic- $\lambda$  structure (**b-d**) and the tetragonal- $\lambda$  structure (**e-h**). The initial and final structures are identical, but three oxygen atoms (A, B, C) are displaced during the drift process. Black arrows on the right indicate the positions of the screw-rotation planes.

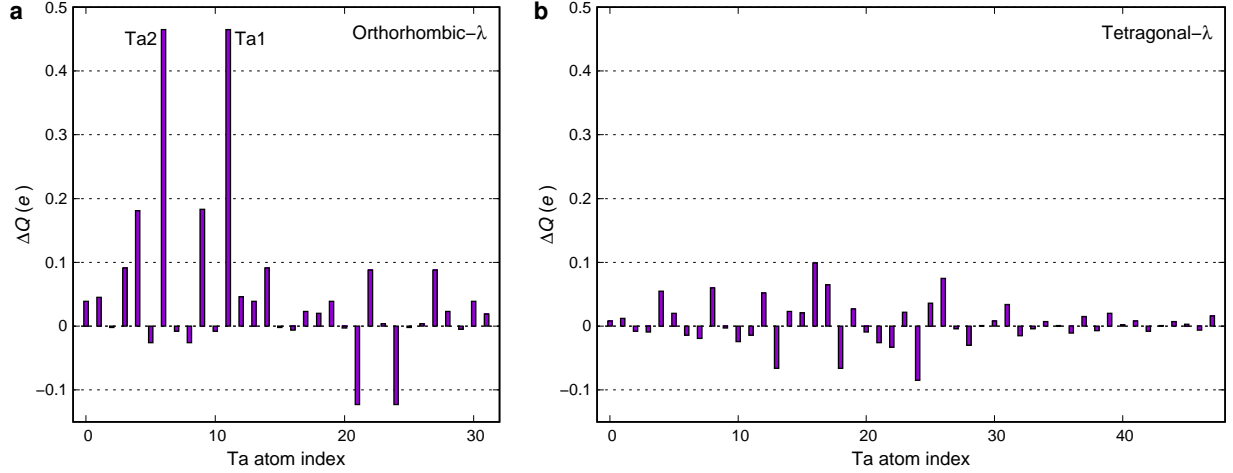


FIG. 4. **Change in Ta atomic charges at the transition state.** **a** Orthorhombic- $\lambda$  structure. Ta1 and Ta2 atoms are specified in Fig. 3c. **b** Tetragonal- $\lambda$  structure. Atomic charges were calculated by projecting the Kohn-Sham eigenstates onto atomic spherical harmonics within a sphere of radius 1.5 Å, as implemented in VASP.  $\Delta Q$  represents the change in atomic charge between the initial state and the transition state, where a positive value indicates an accumulation of electrons.

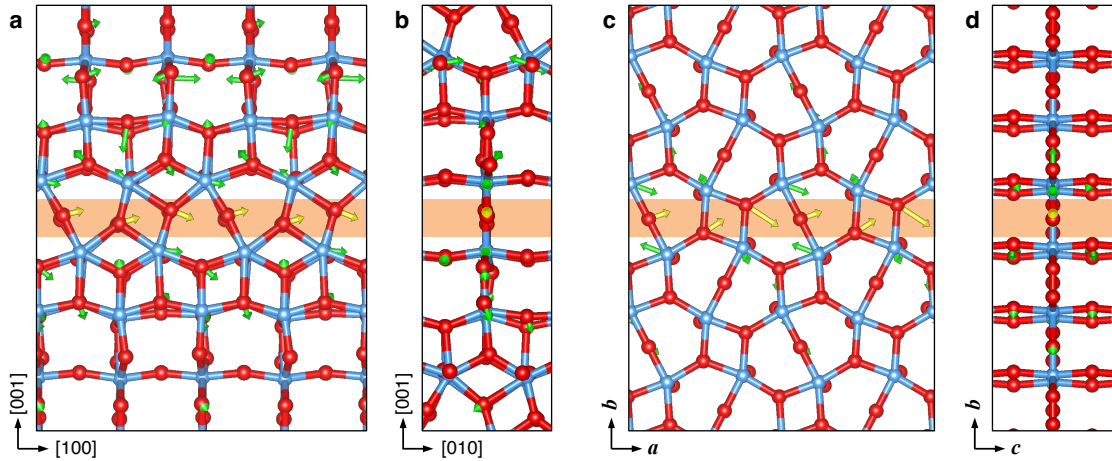


FIG. 5. **Structural relaxation during collective oxygen transport.** **a,b** Atomic displacements from the initial (I) to the first transition (T1) state in the tetragonal- $\lambda$  structure. **c,d** Atomic displacements from the initial (I) to the transition (T) state in the orthorhombic- $\lambda$  structure. Reference structures depict the initial states. Arrows illustrate the displacements of atoms at the transition states: yellow for drifting oxygen atoms (to scale) and green for other atoms (magnified 4 times for clarity).